

Showcasing a new strategy for the synthesis of uniform ultra-small carbon nanospheres (< 50 nm) developed by Prof. Zhibin Ye at Bharti School of Engineering, Laurentian University (Sudbury, Canada).

Synthesis of ultra-small carbon nanospheres (<50 nm) with uniform tunable sizes by a convenient catalytic emulsion polymerization strategy: superior supercapacitive and sorption performance

Ultra-small carbon nanospheres of uniform, easily tunable sizes (10–38 nm) have been synthesized through a new catalytic emulsion polymerization technique and are demonstrated to have superior supercapacitive and sorption performances.

As featured in:



See Zhibin Ye *et al.*,  
*J. Mater. Chem. A*, 2017, 5, 12131.



[rsc.li/materials-a](http://rsc.li/materials-a)

Registered charity number: 207890

Cite this: *J. Mater. Chem. A*, 2017, 5, 12131

# Synthesis of ultra-small carbon nanospheres (<50 nm) with uniform tunable sizes by a convenient catalytic emulsion polymerization strategy: superior supercapacitive and sorption performance†

Vimal K. Tiwari,<sup>a</sup> Zhe Chen,<sup>a</sup> Fan Gao,<sup>b</sup> Zhiyong Gu,<sup>b</sup> Xueliang Sun<sup>c</sup> and Zhibin Ye<sup>id</sup>\*<sup>a</sup>

Porous carbon nanospheres have received enormous attention due to their various applications. Although several elegant strategies exist for the synthesis of relatively large carbon nanospheres (>ca. 100 nm), the synthesis of carbon nanospheres with well-defined, tunable ultra-small sizes (<50 nm) has often been challenging, while such ultra-small nanospheres are much more valuable. A novel, convenient and scalable catalytic emulsion polymerization technique is demonstrated in this paper for the highly efficient synthesis of ultra-small carbon nanospheres with uniform tunable sizes in the range of 11–38 nm. In this strategy, a simple change in the emulsion polymerization recipe renders a convenient yet efficient tuning of the size of the carbon nanospheres. In particular, activated carbon nanospheres (A-CNS21 with an average size of 21 nm), obtained by carbonization in the presence of KOH as the chemical activation agent, possess a very high surface area (2360 m<sup>2</sup> g<sup>-1</sup>) and desired hierarchical macro-/meso-/micropore structures which result from nanosphere packing/aggregation. A-CNS21 is demonstrated to exhibit superior high-rate supercapacitive performance and outstanding sorption capacities towards volatile organic compounds (VOCs), H<sub>2</sub> and CO<sub>2</sub>, which are comparable to or even better than the best results reported to date in these applications. To the best of our knowledge, this is the first synthesis of ultra-small carbon nanospheres, with uniform tunable sizes and superior performance for these applications, by the emulsion polymerization strategy.

Received 5th February 2017  
Accepted 30th March 2017

DOI: 10.1039/c7ta01114h

rsc.li/materials-a

## Introduction

Porous carbon nanospheres (CNSs) have recently received enormous attention towards their applications in energy storage (such as electrical double layer capacitors (EDLCs)), gas storage, organic vapor capture and catalysis.<sup>1</sup> In general, porous CNSs are noted for their greater pore accessibility and faster diffusion of ions/reactants, which are often the common performance parameters that are required for these applications. Because of their small sizes, CNSs tend to aggregate randomly during their preparation to conveniently form desired 3-dimensional hierarchical pore structures that possess high

pore volumes and abundant inter-sphere macropores (>50 nm) and/or mesopores (2–50 nm) besides the intra-sphere micropores (<2 nm).<sup>1,2</sup> In these structures, the intra-sphere micropores contribute to the predominant energy or gas storage capacity,<sup>3,4</sup> while the hierarchical 3-dimensionally inter-connected macropores and mesopores can serve as buffer reservoirs of ions/molecules and facilitate their fast convenient transportation into the micropores.<sup>1,2</sup>

Recent research in the field of carbon nanospheres has focused on the development of synthetic strategies that facilitate the tailored design and synthesis of porous CNSs with high monodispersity, controllable size, high porosity and desirable pore size distribution, high surface area and other structural/composition parameters, in order to meet the application-specific requirements.<sup>1</sup> In this regard, various elegant synthetic strategies have been successfully developed.<sup>1</sup> Some of the most notable strategies include hard templating,<sup>5</sup> organic-organic self-assembly (or soft templating),<sup>6</sup> the extended Stöber method,<sup>7</sup> hydrothermal carbonization<sup>8</sup> and emulsion polymerization.<sup>9</sup> In particular, the former four strategies are the most extensively developed in the literature, but with the carbon

<sup>a</sup>Bharti School of Engineering, Laurentian University, Sudbury, Ontario P3E 2C6, Canada. E-mail: zye@laurentian.ca

<sup>b</sup>Department of Chemical Engineering, University of Massachusetts, Lowell, Massachusetts 01854, USA

<sup>c</sup>Department of Mechanical and Materials Engineering, Western University, London, Ontario N6A 5B9, Canada

† Electronic supplementary information (ESI) available. See DOI: 10.1039/c7ta01114h

precursors narrowly restricted to either thermosetting polymers (mainly phenolic resins) in the former three strategies or to biomass derivatives (such as sugars) in the hydrothermal method. Emulsion polymerization is the most popular versatile and scalable method for producing monodisperse polymer spheres with controllable sizes (such as cross-linked polystyrene spheres).<sup>1a</sup> However, except in the very few cases that incorporate additional special post-synthesis Friedel-Crafts hyper-cross-linking,<sup>9</sup> the method has limited use for the synthesis of porous CNSs due to structural collapse during carbonization and a low carbonization yield resulting from insufficient polymer cross-linking.<sup>9d,e</sup>

In general, CNSs with uniform diameters in the range of *ca.* 100 nm to micrometers have been extensively synthesized utilizing the above strategies.<sup>1,5-9</sup> However, the synthesis of ultra-small CNSs with uniform and precisely tunable diameters of below *ca.* 50 nm (*i.e.*, 10–50 nm) has often been challenging, while such an ultra-small size range is particularly desired for their applications. In EDLC applications, the use of ultra-small CNSs has the advantage of offering short-range intra-sphere micropores, and thus reduced diffusion paths for the ions/molecules in the micropores, as well as better-maintained capacitance retention at high rates.<sup>10,11</sup>

Thus far, ultra-small CNSs with sizes of between 10–50 nm have been synthesized in only very few pioneering reports as follows. In these few cases, although elegant, the ultra-small size range (<50 nm) often represents the lowest end of the large targeted size windows and is thus not the primary focus of the syntheses. In one case, a hard-templated synthesis of mesoporous carbon nanoparticles with sizes of as low as 10 nm was reported, with mesoporous silica used as the template for the carbon precursors.<sup>5c</sup> The synthesis is, however, complicated by the massive use of the silica templates and its tedious removal process. Meanwhile, the ultra-small nanoparticles exhibited a rather poorly defined morphology.<sup>5c</sup> Zhao *et al.* demonstrated an innovative low-concentration synthesis of ordered mesoporous CNSs with uniform tunable sizes within the range of 20–140 nm by the organic–organic self-assembly strategy.<sup>6a</sup> In this case, the very low-concentration synthesis (reactant concentration at  $10^{-7}$  mol L<sup>-1</sup>) is a restriction. Meanwhile, the resulting CNSs were only demonstrated for use in biological applications, but not for use in energy/gas storage or vapor capture applications. Through a seeded Stöber synthetic strategy, Gan *et al.* synthesized CNSs with tunable sizes within the range of 30–90 nm.<sup>7g</sup> However, the process requires inconvenient seed preparation and a very close monitoring of the growth of the seeds for size control. Several reports<sup>8d-g</sup> have demonstrated the synthesis of CNSs with sizes of as low as *ca.* 20–50 nm by the hydrothermal treatment of sugars in the presence of various additives followed by additional carbonization. The CNSs obtained by the hydrothermal method often exhibit an irregular non-spherical morphology, and possess low surface areas and porosities. In addition, Jang *et al.* synthesized ultra-small CNSs with sizes of *ca.* 48 nm from polypyrrole nanospheres prepared by microemulsion polymerization.<sup>9a-c</sup> Those CNSs also possess low surface areas and pore volumes, and have not been demonstrated for use in energy storage or sorption

applications. Lastly, carbon quantum dots with sizes of typically below 10 nm or so have also been synthesized through various techniques.<sup>12</sup> However, they are often restricted to fluorescence-related applications and are not within the scope of the porous CNSs defined herein.

By tackling the restrictions of the existing synthetic methods for ultra-small CNSs, we report in this article a new, convenient and scalable catalytic emulsion polymerization technique for the highly efficient synthesis of a range of ultra-small CNSs with uniform tunable sizes in the specifically targeted range of 10–50 nm from all commercially available precursors. The resulting CNSs have been systematically characterized in terms of their morphological, textural and compositional properties. Meanwhile, the applications of the CNSs as high-rate electrode materials in EDLCs, and as sorbents for the capture of volatile organic compounds (VOCs) and storage of H<sub>2</sub> and CO<sub>2</sub> have been thoroughly investigated. Some superior performances that are comparable to or even better than the best results reported thus far have been successfully demonstrated. To the best of our knowledge, this is the first synthesis, *via* the emulsion polymerization strategy, of ultra-small carbon nanospheres with uniform tunable sizes and superior performances for these applications.

## Experimental

### Materials

1,3-Diethynylbenzene (DEB, 97%, Aldrich), palladium acetate (Pd(OAc)<sub>2</sub>, 98%, Strem Chemicals),  $\alpha,\alpha'$ -bis(di-*t*-butylphosphino)-*o*-xylene (97%, Strem Chemicals), methanesulfonic acid (99.5%, Aldrich), dichloromethane (HPLC grade, Fisher Scientific), methanol (ACS reagent, Fisher Scientific), sodium dodecyl sulphate (SDS,  $\geq 99\%$ , Aldrich), sulfuric acid (96%, Aldrich), titanium foil (99.95%, Aldrich) and conducting carbon (acetylene black 100%, Soltex) were all used as received. Deionized water was obtained from a Barnstead/Synbron Nanopure II water purification system.

### Synthesis of polymer nanospheres (PNSs) by catalytic emulsion polymerization

The following is the typical procedure for the synthesis of PNSs with an average diameter of 21 nm. DEB (1.86 g, 14.7 mmol) was added to a flask containing an aqueous solution of SDS (0.8 g in 15.6 mL of water). The mixture was sonicated for 10 min and then stirred with a magnetic stirrer at 400 rpm for 5 h at 60 °C. A Pd catalyst solution was prepared by dissolving Pd(OAc)<sub>2</sub> (3.31 mg, 14.7  $\mu$ mol) and  $\alpha,\alpha'$ -bis(di-*t*-butylphosphino)-*o*-xylene (17.45 mg, 44  $\mu$ mol) in a mixture of dichloromethane (0.18 mL) and methanol (0.02 mL). The catalyst solution was injected into the monomer emulsion, followed by the addition of two drops of methanesulfonic acid, to start the emulsion polymerization. The polymerization lasted overnight with a maintained stirring speed of 400 rpm at 60 °C, and rendered an intense dark brown emulsion dispersion. As per dynamic light scattering (DLS) analysis of the diluted dispersions, the resulting PNSs had an average size of 21 nm.

For the synthesis of PNSs with an average diameter of 11 nm, DEB (0.93 g, 7.37 mmol) was added to an aqueous solution of SDS (1.0 g in 39 mL of water). The mixture was sonicated and then stirred at 60 °C. A catalyst solution, containing Pd(OAc)<sub>2</sub> (16.55 mg, 73.7 μmol) and  $\alpha,\alpha'$ -bis(di-*t*-butylphosphino)-*o*-xylene (87.25 mg, 221 μmol) in 0.9 mL of dichloromethane and 0.1 mL of methanol, was injected into the monomer emulsion, followed by the addition of four drops of methanesulfonic acid to start the polymerization. The emulsion polymerization lasted overnight under stirring at 400 rpm at 60 °C. DLS analysis of the diluted emulsion showed that the resulting PNSs had an average size of 11 nm.

For the synthesis of PNSs with an average diameter of 38 nm, DEB (1.86 g, 14.7 mmol) was added to an aqueous solution of SDS (0.1 g in 3.9 mL of water) in a flask, followed by sonication and mechanical stirring at 60 °C. A catalyst solution, containing Pd(OAc)<sub>2</sub> (3.3 mg, 15 μmol) and  $\alpha,\alpha'$ -bis(di-*t*-butylphosphino)-*o*-xylene (17.4 mg, 44 μmol) in 0.18 mL of dichloromethane and 0.02 mL of methane, was injected into the monomer emulsion, along with the addition of one drop of methanesulfonic acid. The polymerization lasted overnight at 60 °C under maintained stirring at 400 rpm, and rendered the emulsion product.

### Synthesis of carbon nanospheres by carbonization of polymer nanospheres without or with activation

The PNS emulsions that were prepared as reported above were first hydrothermally treated at *ca.* 220 °C overnight in a Teflon-lined autoclave. The resulting polymer precipitates were collected by filtration, washed with an excessive amount of water and then dried at 60 °C under vacuum for 24 h, thus rendering the hydrothermally treated PNSs (PNS11, PNS21, and PNS38). Direct carbonization of the hydrothermally treated PNSs without activation was carried out by their pyrolysis at 800 °C for 1 h (preceded by heating at a rate of 10 °C min<sup>-1</sup> from 25 to 800 °C) in a nitrogen atmosphere in a tube furnace, thus rendering the non-activated CNSs (CNS11, CNS21, and CNS38, respectively).

For the preparation of KOH-activated carbon nanospheres (A-CNS21), PNS21 and KOH (at 1 : 3 mass ratio) were mixed in methanol, followed by the evaporation of methanol under vacuum. Carbonization was then carried out using the same procedure as described above in a nitrogen atmosphere. To remove any residual KOH, the carbonization product was sequentially washed with a large amount of 2% aqueous HCl solution, deionized water and methanol. It was then dried overnight at 60 °C under vacuum, thus rendering the chemically activated carbon nanospheres, A-CNS21.

### Characterization and measurements

DLS analysis of the diluted emulsions (concentration of *ca.* 0.2 mg mL<sup>-1</sup>), for measuring the sizes of the polymer nanospheres, was carried out using a Malvern Zeta-Sizer Nano S90 instrument at 30 °C. Transmission electron microscopy (TEM) images of the various polymer and carbon nanospheres were captured using a Philips EM400 transmission electron microscope operated at 100 keV. The TEM samples were prepared by

depositing a few drops of the sonicated dilute dispersion of the polymer/carbon nanosphere samples in acetone (*ca.* 0.1 mg mL<sup>-1</sup>) on lacey grids (EMS Supplies), followed by drying. For each sample, about 100 nanospheres were randomly picked and analyzed in order to determine the average nanosphere size and size distribution. Scanning electron microscopy (SEM) images were obtained using a JEOL JSM-7401F field-emission scanning electron microscope. The samples were prepared by depositing a few drops of the dilute dispersion on a small piece of conductive silicon wafer followed by drying at an ambient temperature, and the sample was then mounted to an SEM specimen stub. X-ray diffraction (XRD) patterns of the carbon samples were recorded using an X'Pert Pro diffractometer with Co radiation (wavelength of 1.79 Å) at room temperature. X-ray photoelectron spectroscopy (XPS) measurements of the carbon samples were carried out using a Thermo Scientific Theta Probe XPS spectrometer. A monochromatic Al K $\alpha$  X-ray source was used, with a spot area of 400 μm. Raman spectra were collected using a Renishaw InVia Raman Spectrometer, using a 514 nm laser as the excitation source.

N<sub>2</sub> sorption measurements of the various samples at -196 °C were carried out using a Micromeritics ASAP2020 physisorption analyzer in order to determine the Brunauer-Emmert-Teller (BET) specific surface area, pore volume and pore size distribution. Before the measurements, the samples were degassed for at least 24 h at 100 and 300 °C for the polymer and carbon samples, respectively. The micropore size distribution was calculated from the N<sub>2</sub> sorption data within a relative pressure (*P/P*<sub>0</sub>) range of 0–0.01 with the use of a non-local density functional theory (NLDFT) model. The pore size distribution of the pores with sizes of greater than 20 Å (*i.e.*, mesopores and macropores) was calculated from the N<sub>2</sub> desorption data (*P/P*<sub>0</sub> = *ca.* 0.4–0.99) using the NLDFT model. The sorption isotherms of CO<sub>2</sub> and H<sub>2</sub> with the CNS samples were measured using the same instrument at 0 and -196 °C, respectively. Prior to the measurements, the carbon samples were degassed under vacuum at 300 °C for *ca.* 20 h.

The vapor sorption isotherms of toluene and methanol were obtained using a Belsorp-max instrument (MicrotracBel Corp.) at 25 °C. Prior to the adsorption measurements, the adsorbents (30–50 mg) were degassed under vacuum at 300 °C for *ca.* 20 h. The isotherms were measured from *ca.* 0.01 kPa up to the saturation vapor pressure of the adsorbate at 25 °C.

### EDLC supercapacitor electrode fabrication and electrochemical measurements

All electrochemical measurements of the EDLC supercapacitors, including cyclic voltammetry (CV), galvanostatic charge/discharge (GCD) and electrochemical impedance spectroscopy (EIS), were obtained using a Metrohm Autolab PGSTAT 100 potentiostat/galvanostat in the 2-electrode configuration with aqueous 1 M H<sub>2</sub>SO<sub>4</sub> solution as the electrolyte. The electrodes were fabricated with the various carbon samples on a titanium foil (4 cm<sup>2</sup>) as the current collector. To prepare the electrodes, the active carbon sample (80 wt%), conducting carbon (10 wt%), and Nafion (10 wt%) were dispersed in ethanol

under sonication in a small vial. The dispersion was then evenly coated onto the titanium current collector (active material density of  $1.1 \text{ mg cm}^{-2}$ ). Subsequently, the electrodes were dried in an oven. Symmetrical two-electrode cells were prepared by sandwiching a piece of filtration paper between the two electrodes and were filled with the electrolyte solution. CV measurements were performed in the voltage range of 0–1 V at voltage sweep rates of 200, 50, 25, 10, 5 and  $1 \text{ mV s}^{-1}$ . The specific capacitance ( $C_{\text{sp}}$  in  $\text{F g}^{-1}$ ) was calculated from the CV curves using the following equation:

$$C_{\text{sp}} = \frac{\int i dV}{m \Delta V \nu} \quad (1)$$

where  $i$  and  $V$  are the current and voltage, respectively, in the CV curves,  $m$  is the mass of active carbon in one single electrode, and  $\nu$  is the voltage sweep rate. GCD measurements were performed within the voltage range of 0–1 V at current densities of 50, 30, 20, 10, 5, 3, 2, 1, 0.5, 0.25 and  $0.1 \text{ A g}^{-1}$ .  $C_{\text{sp}}$  was also calculated from the discharge curve using the following equation:

$$C_{\text{sp}} = \frac{2i}{m dV/dt} \quad (2)$$

where  $i$  is the discharge current,  $m$  is the carbon mass in each electrode, and  $dV/dt$  is calculated from the slope of the discharge curve within the voltage range following the end of the ohmic drop to the end of the discharge curve. The energy density ( $E$ , in  $\text{W h kg}^{-1}$ ) and power density ( $P$ ,  $\text{W kg}^{-1}$ ) were calculated according to:

$$E = \frac{1}{2} C_{\text{sp}} V^2 \frac{1}{4} \frac{1}{3.6} \quad (3)$$

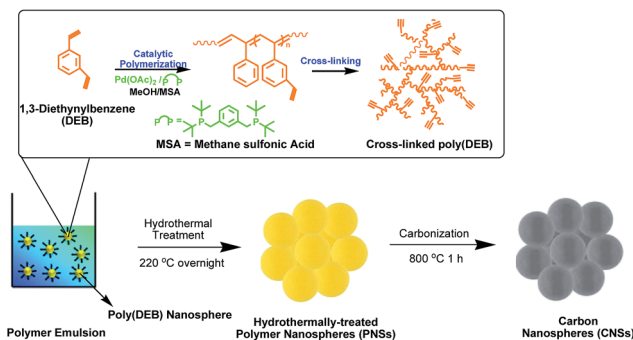
$$P = \frac{E}{t} \quad (4)$$

where  $V$  is the cell voltage after the ohmic drop and  $t$  is the discharge time (in h). The EIS measurements were also conducted at a static potential of 0 V over a frequency range from 10 kHz to 0.01 Hz with an AC perturbation of 10 mV.

## Results and discussion

### Synthesis and characterization of carbon nanospheres by catalytic emulsion polymerization

The synthesis of the ultra-small CNSs reported herein involves three steps: (1) catalytic emulsion polymerization of 1,3-diethynylbenzene (DEB), (2) simple hydrothermal treatment of the resulting polymer nanospheres and (3) carbonization of the polymer nanospheres. This involves the exclusive use of commercially available precursors. Scheme 1 illustrates schematically the synthetic procedure. Unique to this strategy, DEB, a difunctional cross-linkable alkyne monomer (molecular formula  $\text{C}_8\text{H}_6$ ) which possesses a high carbon content (95 wt%), is employed as the monomer precursor for the catalytic emulsion polymerization. This differs from the traditional synthesis of CNSs by emulsion polymerization, where styrenics (divinylbenzene and styrene, with the former used as the cross-linker) are commonly employed for the emulsion synthesis of cross-



Scheme 1 Schematic showing the synthesis of carbon nanospheres by catalytic emulsion polymerization of DEB.

linked styrenic PNSs *via* a radical mechanism.<sup>9d,e</sup> However, styrenic PNSs often undergo severe structural collapse during carbonization due to limited cross-linking density,<sup>9d,e</sup> and possess a low carbon yield. On the contrary, we have shown in our recent work that the Pd-catalyzed coordinative addition polymerization of DEB can efficiently yield non-nanostructured and highly cross-linked polymers, which can subsequently give rise to porous carbons with particle sizes in the micrometer range in high yield (83%) by simple pyrolysis.<sup>13</sup> This desirable feature encourages us to develop ultra-small carbon nanospheres from poly(DEB) nanospheres produced from DEB as the monomer precursor by emulsion polymerization.

In this method, emulsion polymerization of DEB was carried out at  $60 \text{ }^\circ\text{C}$  with the use of an *in situ* generated cationic diphosphine-ligated Pd catalyst,  $\text{Pd}(\text{OAc})_2/\alpha, \alpha'$ -bis(di-*tert*-butylphosphino)-*o*-xylene/methanesulfonic acid.<sup>14</sup> Due to its low oxophilicity, the catalyst is extremely active despite being in polar aqueous media,<sup>15</sup> and requires only a very low Pd loading ( $[\text{Pd}]/[\text{DEB}]$  ratio as low as 1/3000). SDS was used as the surfactant with its concentration in the range of  $0.025\text{--}0.05 \text{ g mL}^{-1}$ , which is far greater than its critical micelle concentration of *ca.*  $0.0029 \text{ g mL}^{-1}$ , so as to achieve miniemulsions.<sup>16</sup> In this emulsion polymerization system, the micelles that contain DEB act as nano-scale reactors, thus rendering poly(DEB) PNSs. For this system, we have found that a change in the SDS concentration in the above range causes no pronounced effects on the size of the resulting PNSs. Instead, the feed concentration of DEB monomer in water has the predominant effect on the size of the PNSs. Efficient tuning of the size of the PNSs can be conveniently achieved by simply changing the DEB feed concentration in water. As a demonstration, a range of PNSs with three different average sizes (PNS11, PNS21 and PNS38 with average diameters of 11, 21 and 38 nm, respectively, as determined by DLS and/or TEM characterizations) were synthesized at different DEB concentrations of 0.024, 0.12 and  $0.48 \text{ g mL}^{-1}$ , respectively. This range of monomer feed concentration is about an order of magnitude higher than that used in the low-concentration synthesis of ultra-small mesoporous CNSs by Zhao *et al.*,<sup>6a</sup> thus indicating significantly enhanced productivity herein. Particle size analysis of the three as-produced PNS miniemulsions by both DLS and TEM analysis

confirmed their average sizes and the very narrow size distribution (polydispersity index of as low as 0.02 and 0.08 for PNS11 and PNS21, respectively, as per DLS analysis; see Fig. S1 in the ESI†).

The resulting emulsions containing the PNSs were subsequently treated hydrothermally at *ca.* 220 °C. We found that the hydrothermal treatment rendered the resulting CNSs with better-retained nanosphere morphology during the subsequent carbonization, which is attributed to the further enhanced cross-linking density within the PNSs by continued polymerization reactions at the elevated temperature during hydrothermal treatment. Meanwhile, the treatment also decomposes/destabilizes the SDS and facilitates its easy removal through simple washing, while it is otherwise difficult to remove the SDS from the as-produced emulsions even by extensive washing. From analysis of the weights of the hydrothermally treated PNSs, DEB conversion during the emulsion polymerizations was found to be nearly quantitative (over 90% in all cases). The hydrothermally treated PNSs were then carbonized at 800 °C for 1 h under a N<sub>2</sub> atmosphere in the absence of any activation agent in order to render the CNSs (CNS11, CNS21 and CNS38, respectively, with the number representing the average size of the CNSs). Relative to the PNS precursors, the yield of CNSs was about 80 wt%, which is very high relative to many other polymer precursors.<sup>13</sup> This confirms the very high atomic efficiency for the conversion of poly(DEB) to carbon.

Fig. 1 shows TEM images of the hydrothermally treated PNSs and their resulting CNSs. Fig. S2 in the ESI† shows SEM images of PNS21 and CNS21 as representative samples. All of the PNS and CNS samples are composed of aggregates/compacts of well-defined nanospheres with very uniform sizes. Commonly observed with various carbon nanospheres, such packing/aggregation is highly desirable, and generates the valuable hierarchical macro-/meso-/micropore structures in the carbon materials which facilitate their applications as superior high-rate electrode materials and fast-adsorbing sorbents. In the case of PNS11 and CNS11, aggregation of the nanospheres is more severe compared to the others, with a fraction of fused nanospheres observed in CNS11, which is expected due to them possessing the smallest nanosphere sizes. By analyzing more than 100 nanospheres from the TEM images of each sample, the average sizes of the PNS samples were found to agree well with those determined by DLS analysis of the as-produced emulsions, thus indicating that the hydrothermal treatment had no pronounced effect on the size of the polymer nanospheres. Meanwhile, the resulting CNSs also have nearly identical average nanosphere sizes to the corresponding PNS precursors, with no obvious deterioration in the nanosphere morphology during carbonization. The TEM and SEM images solidly confirm the successful synthesis of CNSs with well-defined and easily tunable ultra-small sizes in the desired range of 11–38 nm by this catalytic emulsion polymerization strategy.

N<sub>2</sub> sorption characterization of the CNS samples (CNS11, CNS21 and CNS38), as well as PNS21 as a representative PNS sample, was carried out at –196 °C. Fig. 2(a) shows the N<sub>2</sub> sorption isotherms of the samples, with the results summarized in Table 1. Generally, the samples (CNS samples and PNS21) all

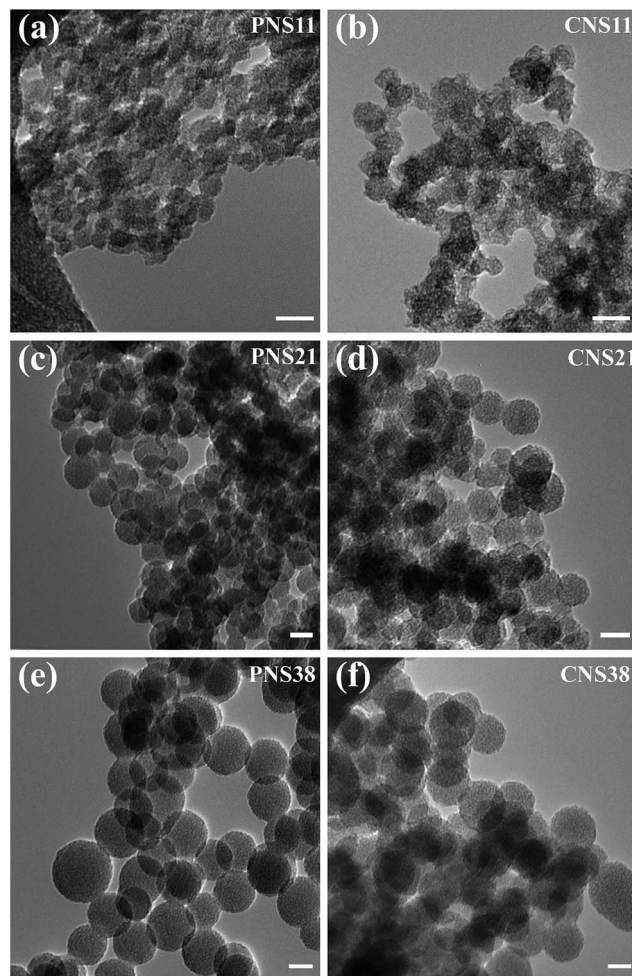


Fig. 1 TEM images of the polymer nanospheres (PNS11, PNS21 and PNS38) and their corresponding carbon nanospheres (CNS11, CNS21 and CNS38) obtained by carbonization at 800 °C for 1 h. Scale bar = 20 nm.

show typical type IV isotherms,<sup>17</sup> with a slight uptake in the low relative pressure range ( $P/P_0 < 0.1$ ), a sharp uptake at the high relative pressure end ( $0.8 < P/P_0 < 1$ ) and the presence of a distinct hysteresis loop in the  $P/P_0$  range of 0.8–1. Except for CNS11 which shows a hysteresis loop intermediate between types H1 and H3, PNS21, CNS21 and CNS38 all show a type H1 hysteresis loop,<sup>17</sup> with the two branches being almost vertical and parallel over an appreciable range of N<sub>2</sub> uptake. The type H1 hysteresis is often associated with agglomerates/compacts of approximately uniform spheres in a fairly regular array.<sup>17</sup> This also confirms the presence of uniform nanospheres in these samples (PNS21, CNS21 and CNS38) and suggests their relatively regular packing to form narrow-distributed inter-nanosphere pores. On the contrary, the type H3 hysteresis loop is often observed in aggregates of plate-like particles that give rise to slit-shaped pores.<sup>17</sup> The intermediate hysteresis loop in CNS11 is indicative of the presence of a fraction of plate-like particles that are formed by the fusion of nanospheres during carbonization, which is in agreement with the findings demonstrated in its TEM image (Fig. 1(b)).

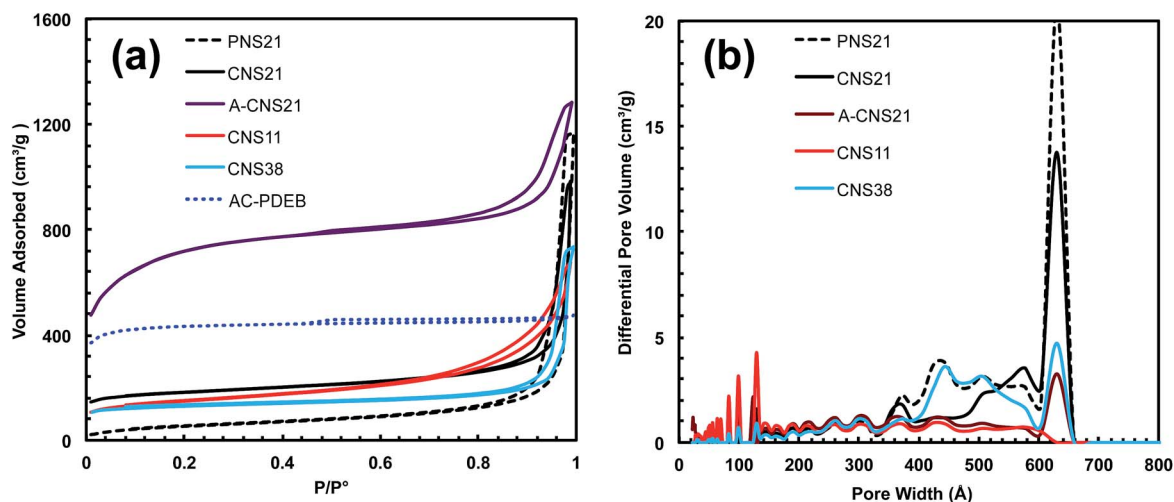


Fig. 2 (a)  $N_2$  sorption curves of various CNS and PNS samples; (b) their mesopore/macropore size distribution curves, as determined using the NLDFT model.

The polymer nanospheres in PNS21 appear to be solid with negligible intra-sphere micropores, given the marginal  $N_2$  uptake at the low relative pressure range. It has a low BET surface area of  $199 \text{ m}^2 \text{ g}^{-1}$ , with a negligible micropore surface area, and a high total pore volume of  $1.80 \text{ cm}^3 \text{ g}^{-1}$  which arises exclusively from the inter-sphere mesopores/macropores that are generated by the packing/aggregation of nanospheres. The carbon nanospheres in the CNS samples (CNS11, CNS21 and CNS38) have a total BET surface area of 493, 580 and  $407 \text{ m}^2 \text{ g}^{-1}$ , respectively, and a total pore volume of 1.04, 1.52 and  $1.13 \text{ cm}^3 \text{ g}^{-1}$ , respectively (see Table 1). They possess significant intra-sphere micropores, with the micropore surface area contributing about 60% of the surface area in CNS21 and CNS38, and 33% in CNS11. However, the majority (90%) of the pore volume arises from the inter-sphere mesopores/macropores that are generated by the packing/aggregation of the CNSs. Fig. 2(b) compares the mesopore/macropore size distributions of the samples, obtained using the NLDFT model. PNS21, CNS21 and CNS38 have the pore size distribution primarily in the narrow range of 40–66 nm, with similar average mesopore/macropore sizes (44.3, 41.6 and 40.7 nm, respectively). In particular, CNS21 has a similar distribution pattern to its precursor PNS21

and both have a peak distribution intensity at 63 nm. However, CNS11 shows a broader distribution within the 2–60 nm range, with a peak distribution intensity at around 12 nm and a lowered average mesopore/macropore size of 26.1 nm.

Fig. S3 in the ESI† shows the XRD pattern of CNS21 as a representative sample. There is an intense diffraction peak with a peak maximum at *ca.*  $3.9^\circ$ , thus indicating the presence of high-density pores within the carbon material.<sup>13</sup> In addition, a broad weak peak is present at around  $28^\circ$ , which is attributed to the (002) peak of graphitic structures.<sup>18–20</sup> The weak and broad nature of the peak indicates a low degree of graphitization in the carbon material. As expected, this is typical of amorphous carbon materials that are prepared by pyrolysis at a relatively low temperature due to insufficient graphitization.<sup>19</sup> An increase in the pyrolysis temperature is expected to improve the graphite content, which will be investigated in subsequent studies.

The above CNS samples produced by carbonization without activation all possess relatively low surface areas and insufficient numbers of micropores. To obtain carbon nanospheres with enhanced surface areas for applications in high-capacitance supercapacitor electrode materials or high-

Table 1 Textural properties of the polymer/carbon samples determined by  $N_2$  sorption at  $-196^\circ \text{C}$

Sample	Surface area <sup>a</sup> ( $\text{m}^2 \text{ g}^{-1}$ )			Pore volume <sup>b</sup> ( $\text{cm}^3 \text{ g}^{-1}$ )			Average pore size <sup>c</sup> (Å)	
	$S_{\text{BET}}$	$S_{\text{micro}}$	$S_{\text{meso/macro}}$	$V_{\text{total}}$	$V_{\text{micro}}$	$V_{\text{meso/macro}}$	$d_{\text{meso/macro}}$	$d_{\text{micro}}$
PNS21	199	0	199	1.80	0	1.80	443	
CNS21	580	323	256	1.52	0.17	1.35	416	7.3
CNS11	493	165	327	1.04	0.09	0.95	261	8.3
CNS38	407	249	158	1.13	0.13	1.00	407	8.0
A-CNS21	2360	882	1477	1.98	0.46	1.52	268	9.1
AC-PDEB	1308	1081	228	0.73	0.57	0.16		8.0

<sup>a</sup> BET surface area ( $S_{\text{BET}}$ ), as well as the surface area of the micropores ( $S_{\text{micro}}$ ) and mesopores/macropores ( $S_{\text{meso/macro}}$ ), determined using the *t*-plot method. <sup>b</sup> Total pore volume ( $V_{\text{total}}$ ), as well as the micropore volume ( $V_{\text{micro}}$ ) and mesopore/macropore volume ( $V_{\text{meso/macro}}$ ), determined using the *t*-plot method. <sup>c</sup> Average micropore size ( $d_{\text{micro}}$ ) and mesopore/macropore size ( $d_{\text{meso/macro}}$ ), determined using the NLDFT model.

capacity sorbents, we also prepared a KOH-activated carbon nanosphere sample, A-CNS21, by simply carbonizing PNS21 in the presence of KOH (at a KOH/PNS21 mass ratio of 3/1) as the chemical activation agent under N<sub>2</sub> at 800 °C for 1 h. Fig. 3(a) shows a TEM image of A-CNS21. The nanosphere morphology is still clearly observable in the TEM image. Its N<sub>2</sub> sorption isotherm is also shown in Fig. 2(a). A strong uptake is seen in the low relative pressure range, which is indicative of the significant presence of micropores, along with a hysteresis loop intermediate between types H1 and H3 within the relative pressure range of 0.7–1. It has a high BET surface area of 2360 m<sup>2</sup> g<sup>-1</sup> and a high total pore volume of 1.98 cm<sup>3</sup> g<sup>-1</sup>, which are both dramatically enhanced relative to the non-activated CNS21. Meanwhile, it also possesses a significant micropore size surface area (882 m<sup>2</sup> g<sup>-1</sup>; 37% of the total surface area) and micropore volume (0.46 cm<sup>3</sup> g<sup>-1</sup>; 23% of the total pore volume).

Clearly, the use of KOH as the activation agent is highly efficient for generating significant intra-sphere micropores and mesopores. Compared to CNS21, its average mesopore/macropore size is slightly reduced to 26.8 nm, due to the creation of small intra-sphere mesopores and the narrowing of some of the inter-sphere mesopores/macropores upon activation. Nevertheless, like CNS21, A-CNS21 shows a peak distribution intensity at 63 nm in the mesopore/macropore size distribution curve (see Fig. 2(b)), thus confirming the significant retention of the nanosphere morphology despite chemical activation. Its textural/pore structures make A-CNS21 resemble carbon aerogels that are prepared by sol-gel routes.<sup>2e</sup>

For the purpose of comparison, we have also synthesized an activated carbon control sample, AC-PDEB, from the non-nanostructured cross-linked polymer of DEB (PDEB) synthesized in our previous work<sup>13</sup> as the polymer precursor with the same chemical composition as PNS21. Unlike PNS21, PDEB, synthesized by conventional catalytic polymerization in organic media, does not contain designed nano-structures. TEM analysis shows that it exhibits irregular large sizes (ca. 1–10 μm).<sup>13</sup> AC-PDEB was obtained by carbonization of PDEB in the presence of KOH under identical conditions as those used for the preparation of A-CNS21. Fig. 3(b) shows a TEM image of AC-PDEB, in which irregular particles with dimensions in the range of around 0.2 μm to a few microns can be seen. AC-PDEB shows a type I isotherm with a negligibly small hysteresis loop (see Fig. 2(a)) and is thus predominantly microporous with

marginal meso-/macropore structures. This marks its distinct difference from A-CNS21, synthesized from nanostructured PNSs, which possesses hierarchical macro-/meso-/micropore structures. AC-PDEB has a BET surface area of 1308 m<sup>2</sup> g<sup>-1</sup> and a total pore volume of 0.73 cm<sup>3</sup> g<sup>-1</sup>, with the majority (83 and 78%, respectively; see Table 1) arising from micropores. As per micropore analysis, carried out *via* the NLDFT model, A-CNS21 has a slightly higher average micropore size (9.1 vs. 8.0 Å) than AC-PDEB (see Fig. S4 in the ESI† for the micropore size distribution).

Both A-CNS21 and AC-PDEB were characterized using XPS in order to determine their chemical compositions and chemical identities. The atomic composition survey reveals that A-CNS21 contains C at ca. 92 atom% and O at 7 atom%, while AC-PDEB possesses corresponding contents of 95 and 4 atom%, respectively (see Fig. S5 in the ESI†). The slightly higher O content in A-CNS21 than in AC-PDEB should result from the inter-sphere mesopores/macropores present in PNS21, which facilitate the deeper and more uniform penetration of KOH for enhanced chemical activation. Fig. S6 in the ESI† shows the Raman spectra of PNS21, A-CNS21 and AC-PDEB. While PNS21 exhibits no Raman peak in the given region, both A-CNS21 and AC-PDEB show similar spectra with broad overlapping D and G bands centered at 1350 and 1588 cm<sup>-1</sup>, respectively. The intensity ratio of the D and G bands is 0.88 and 0.94 for A-CNS21 and AC-PDEB, respectively, thus suggesting a low degree of graphitization of the carbons.<sup>5c</sup>

AC-PDEB is employed as the activated carbon control sample in our subsequent study of the performance of A-CNS21 as an EDLC electrode material, and as a sorbent for CO<sub>2</sub>/H<sub>2</sub> storage and the capture of VOCs. We reason that AC-PDEB, synthesized from polymer precursors with identical chemical compositions *via* the same procedure as A-CNS21, should serve this purpose better than other commercial activated carbons. Compared to AC-PDEB synthesized herein, commercial activated carbons are often obtained from complex natural precursors by different pyrolysis treatment procedures.

### Electrochemical supercapacitive performance

Due to their hierarchical pore structures and ultra-small nanosphere size, the high-surface-area CNSs synthesized through our catalytic emulsion polymerization strategy are reasoned to be promising superior electrode materials for use in EDLCs with high capacitance and capacitance retention at high currents. As a proof-of-concept demonstration, A-CNS21 has been thoroughly evaluated herein for its electrochemical supercapacitive performance in a two-electrode symmetrical cell in 1 M H<sub>2</sub>SO<sub>4</sub> aqueous electrolyte. CV, GCD and EIS measurements were carried out, with the results summarized in Fig. 4 and Fig. S7 in the ESI.† The CV curves shown in Fig. 4(a) exhibit typical rectangular shapes even at the high voltage sweep rate of 200 mV s<sup>-1</sup>, along with only small reductions in the areas of the rectangles observed upon gradually increasing the voltage sweep rate from 5 to 200 mV s<sup>-1</sup>. This is indicative of the ideal capacitive behavior and excellent capacitance retention at high sweep rates. The specific capacitance calculated

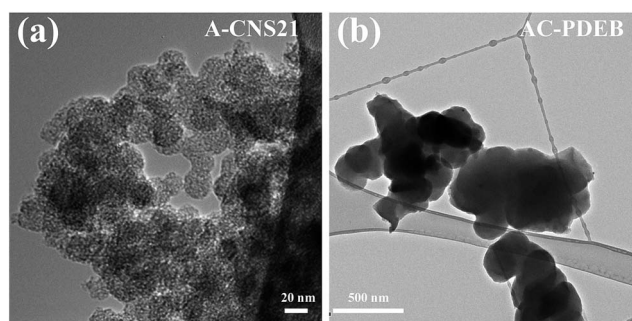
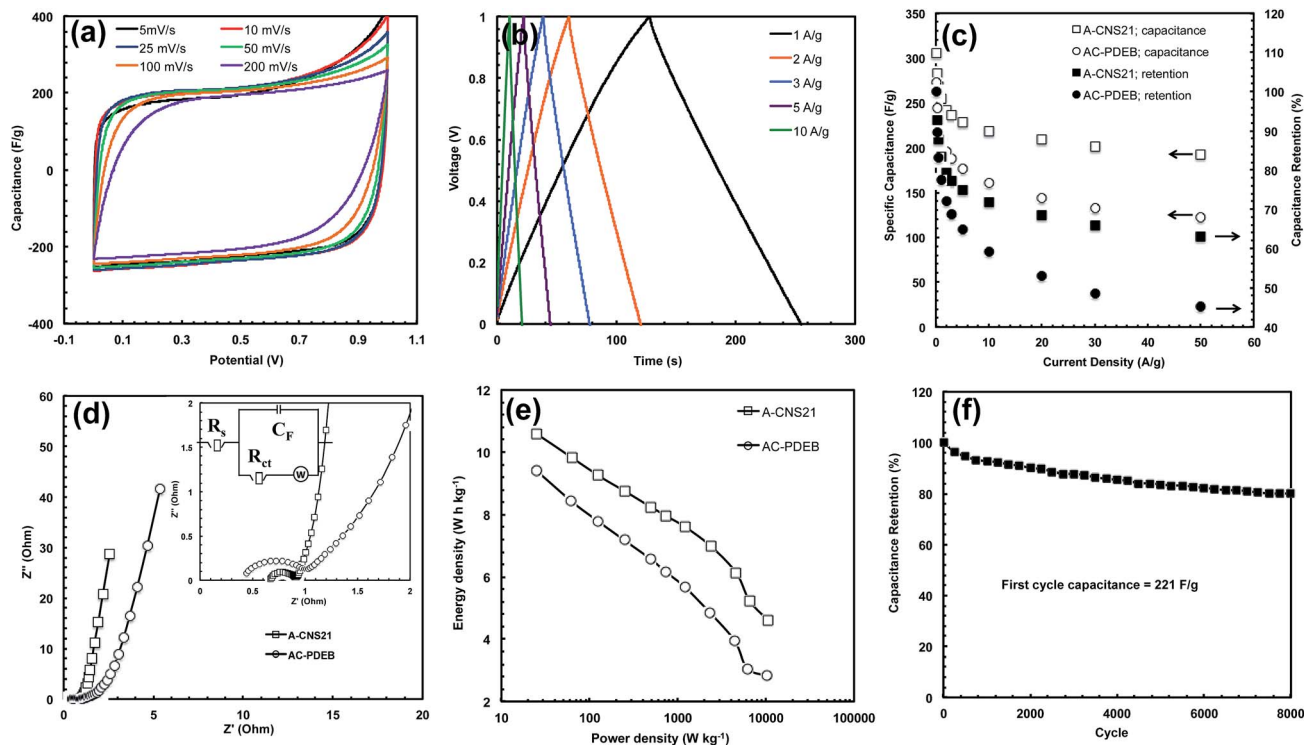


Fig. 3 TEM images of (a) A-CNS21 and (b) AC-PDEB.



**Fig. 4** Electrochemical supercapacitive results of A-CNS21 in a two-electrode cell configuration in 1 M H<sub>2</sub>SO<sub>4</sub> aqueous electrolyte: (a) CV curves at different voltage sweep rates; (b) GCD curves at different current densities (1–10 A g<sup>-1</sup>); (c) specific capacitance and capacitance retention as functions of current density; (d) Nyquist plot with the inset showing the high frequency region and the electrical equivalent circuit used for fitting the impedance spectra; (e) Ragone plot; (f) cyclic stability at the current density of 5 A g<sup>-1</sup> over 8000 charge–discharge cycles. The results of AC-PDEB under identical measurement conditions are included in (c)–(e) for comparison.

from the CV curves decreases only slightly from 214 F g<sup>-1</sup> at 5 mV s<sup>-1</sup> to 167 F g<sup>-1</sup> at 200 mV s<sup>-1</sup>, representing a 78% capacitance retention at 200 mV s<sup>-1</sup>. In contrast, the CV curves of AC-PDEB (see Fig. S8(a) in the ESI<sup>†</sup>) show increasingly obvious distortions from the rectangular shape with increasing sweep rates, along with a pronounced decrease in the enclosed area. Its specific capacitance calculated from the CV curves shows a severe drop from 187 F g<sup>-1</sup> at 5 mV s<sup>-1</sup> to 101 F g<sup>-1</sup> at 200 mV s<sup>-1</sup>, representing only 54% retention.

The GCD curves of A-CNS21 (see Fig. 4(b) and S7<sup>†</sup>) also exhibit the triangular shapes that are typically found for ideal capacitors. The voltage drops in the discharge curves resulting from equivalent series resistance are favorably small (*e.g.*, only 0.068 V at 10 A g<sup>-1</sup>). Fig. 4(c) plots the specific capacitance and capacitance retention obtained from the GCD measurements at different current densities. A high specific capacitance of 305 F g<sup>-1</sup> is obtained at 0.1 A g<sup>-1</sup>, with only slight decreases to 255 and 219 F g<sup>-1</sup> at 1 and 10 A g<sup>-1</sup>, respectively. On the contrary, the specific capacitance values of AC-PDEB are 273, 211 and 160 F g<sup>-1</sup> at the three corresponding current densities. Meanwhile, the percentages of capacitance retention of A-CNS21 at various high current densities far exceed those of AC-PDEB. For example, in reference to the specific capacitance at 0.1 A g<sup>-1</sup>, a 72% capacitance retention is achieved for A-CNS21 at 10 A g<sup>-1</sup> while the corresponding retention is 58% for AC-PDEB. The high specific capacitance and capacitance retention values

achieved herein for A-CNS21 exceed or compare well to those of many other high-performance porous carbons (see Table S1 in the ESI<sup>†</sup>). For example, the high-performance hollow carbon nanospheres (outer diameter: 69 nm) with an ultra-high surface area (3022 m<sup>2</sup> g<sup>-1</sup>) that were developed elegantly by Wu *et al.* were reported to demonstrate specific capacitance values of 203, 180 and 153 F g<sup>-1</sup> at 0.1, 1 and 10 A g<sup>-1</sup>, respectively, which are appreciably lower than the values obtained herein for A-CNS21, although with similar capacitance retentions.<sup>6f</sup> However, unlike A-CNS21, the synthesis of hollow carbon nanospheres therein requires extremely long high-temperature carbonization (20 h) and a precisely controlled temperature ramping rate, which may be challenging for its applications.

Fig. 4(d) compares the Nyquist plots of A-CNS21 and AC-PDEB, obtained from EIS measurements within the frequency range of 10 kHz to 0.01 Hz. The equivalent circuit for the fitting of the EIS data is included therein, where  $R_s$  is the intrinsic ohmic resistance,  $C_F$  is a double-layer capacitor,  $R_{ct}$  is the faradaic charge transfer resistance, and  $W$  is the Warburg impedance. Both carbons show a distinct semicircle at high frequency and a nearly vertical line at low frequency. In the plot of AC-PDEB, an additional long inclined Warburg-type line (with a slope of about 45°; see the inset in Fig. 4(d)) is present at an intermediate frequency while it is nearly absent in the plot of A-CNS21. It is known that the semicircle corresponding to the faradaic charge-transfer resistance arises primarily from the ion

transport within the mesopores and the Warburg-type line is ascribed to the ion movement within the micropores.<sup>19b</sup> Herein, the semicircle of A-CNS21 is much smaller (0.227  $\Omega$ ) than that (0.553  $\Omega$ ) of AC-PDEB (see the inset in Fig. 4(d)), thus indicating the significantly lowered ion transport resistance within the mesopores in A-CNS21 due to the presence of abundant mesopore volume within the hierarchical structures. Meanwhile, the absence of the Warburg line in A-CNS21 also confirms the dramatically reduced ion transfer resistance within its intra-sphere micropores due to the shortened diffusion length as a result of the ultra-small nanosphere size and/or the presence of intra-sphere mesopores. The intrinsic ohmic resistance (the first intercept of the semicircle along the real axis) of A-CNS21 is slightly higher than that of AC-PDEB (0.67 vs. 0.44  $\Omega$ ), thus indicating the slightly lower conductivity of A-CNS21 due to the higher porosity. However, the equivalent series resistance (ESR), obtained by extrapolating the vertical portion in the low-frequency region, is significantly lower in A-CNS21 than in AC-PDEB (1.16 vs. 2.54  $\Omega$ ). The difference of 1.38  $\Omega$  between the two ESR values should result from the smaller charge transfer resistance and, more importantly, the faster ion diffusion within the shorter micropores in A-CNS21.

The Ragone plot (see Fig. 4(e)) shows that a high energy density of 10.6 W h kg<sup>-1</sup> is achieved with A-CNS21, which is much higher than that of a common carbon electrode (5 W h kg<sup>-1</sup>).<sup>6f</sup> A cyclic stability test was carried out on a two-electrode cell fabricated with A-CNS21 for 8000 GCD cycles at 5 A g<sup>-1</sup>. Fig. 4(f) plots the capacitance retention curve. About 80% of the initial capacitance (221 F g<sup>-1</sup>) is retained after 8000 cycles, thus confirming its excellent cyclic stability.

### VOC sorption performance

With its high surface area and pore volume, A-CNS21 with hierarchical pore structures is also highly attractive for the adsorption of VOCs that are of serious environmental concern. Herein, its adsorption properties towards the vapor of two

representative VOCs, toluene and methanol, have been investigated, along with AC-PDEB for comparison. Fig. 5 shows adsorption isotherms measured at 25 °C, with the adsorption capacity at different relative vapor pressures ( $P/P_0$ ) summarized in Table 2. In the figure, it can be seen that both A-CNS21 and AC-PDEB exhibit type I isotherms for the adsorption of both toluene and methanol vapors. A-CNS21 shows maximum adsorption capacities of 967 and 937 mg g<sup>-1</sup> for toluene and methanol, respectively, at a  $P/P_0$  of 0.99. These maximum capacity data are very high and compare well with those of many other porous materials studied for organic vapor adsorption (see Table S2 in the ESI†), such as porous carbons (456–1500 mg g<sup>-1</sup> and 243–1230 mg g<sup>-1</sup> for toluene and methanol, respectively), microporous polymers (780–1357 mg g<sup>-1</sup> and 289–934 mg g<sup>-1</sup> for toluene and methanol, respectively), and metal organic frameworks (MOFs, 125–1285 mg g<sup>-1</sup> and 100–480 mg g<sup>-1</sup> for toluene and methanol, respectively).<sup>6f</sup> Among the various porous carbons reported for the adsorption of toluene and methanol vapors, the maximum adsorption capacity data achieved with A-CNS21 herein are the second highest, and are only lower than those (1500 and 1230 mg g<sup>-1</sup> for toluene and methanol, respectively) reported for the hollow carbon nanospheres with an ultra-high surface area developed by Wu *et al.*<sup>6f</sup>

Most distinctively, A-CNS21 shows an extremely high adsorption capacity for both toluene and methanol within the low  $P/P_0$  range ( $P/P_0 < 0.1$ ), with very steep isotherms. At a  $P/P_0$  of 0.01, it exhibits adsorption capacities of 159 and 21 mg g<sup>-1</sup> towards toluene and methanol, respectively. At a  $P/P_0$  of 0.05, the capacities are 585 and 167 mg g<sup>-1</sup> towards toluene and methanol, respectively. Upon further increasing  $P/P_0$  to 0.1, the values reach 866 and 366 mg g<sup>-1</sup> towards toluene and methanol, respectively. These data suggest the highly responsive capture of VOCs at a low  $P/P_0$  range. Beyond this range (*i.e.*,  $P/P_0 > 0.1$ ), the toluene adsorption capacity (951 mg g<sup>-1</sup>) is almost saturated at a  $P/P_0$  of 0.27, with only a marginal increase observed afterwards, while for methanol, the adsorption

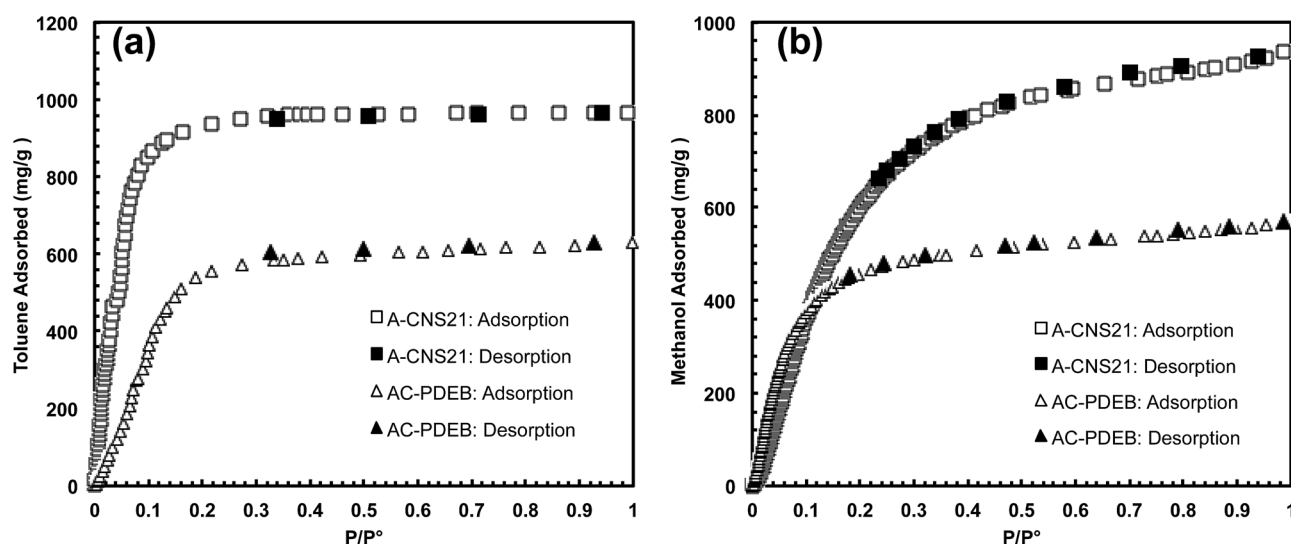


Fig. 5 Sorption isotherms of A-CNS21 and AC-PDEB towards the vapors of toluene (a) and methanol (b) at 25 °C.

Table 2 Vapor and gas adsorption capacity data

Sample	Methanol adsorption capacity (in mg g <sup>-1</sup> ) at different $P/P_0$ <sup>a</sup>				Toluene adsorption capacity (in mg g <sup>-1</sup> ) at different $P/P_0$ <sup>a</sup>				CO <sub>2</sub> adsorption capacity <sup>b</sup> (wt%)	H <sub>2</sub> adsorption capacity <sup>c</sup> (wt%)
	$P/P_0 = 0.01$	$P/P_0 = 0.05$	$P/P_0 = 0.1$	$P/P_0 = 0.99$	$P/P_0 = 0.01$	$P/P_0 = 0.05$	$P/P_0 = 0.1$	$P/P_0 = 0.99$		
A-CNS21	21	167	366	937	159	585	866	967	26	2.5
AC-PDEB	46	250	380	572	38	163	366	631	28	2.4

<sup>a</sup> Methanol and toluene adsorption capacity measured at 25 °C. <sup>b</sup> CO<sub>2</sub> sorption capacity measured at 0 °C and 1 bar. <sup>c</sup> H<sub>2</sub> sorption capacity measured at -196 °C and 1 bar.

capacity still shows a continuous increase, although at reduced rates, upon further increasing  $P/P_0$ .

The excellent adsorption capacities of A-CNS21 towards toluene and methanol vapors at a low  $P/P_0$  (<0.1) are even better than those of various types of high-performance sorbents that exhibit higher maximum adsorption capacities (see Table S2†). For example, although they exhibit strikingly high maximum adsorption capacities, the hollow carbon nanospheres developed by Wu *et al.* exhibit adsorption capacities of *ca.* 800 and 240 mg g<sup>-1</sup> towards toluene and methanol, respectively, at a  $P/P_0$  of 0.1,<sup>6f</sup> which are lower than the corresponding values (866 and 366 mg g<sup>-1</sup> towards toluene and methanol, respectively) of A-CNS21. In another example, a mesoporous aromatic framework exhibited a toluene adsorption capacity of *ca.* 800 mg g<sup>-1</sup> at a  $P/P_0$  of 0.1, although it exhibits an excellent maximum adsorption capacity of 1355 mg g<sup>-1</sup> towards saturated toluene vapor.<sup>21</sup> Compared to a well-known MOF, HKUST-1, with a remarkable toluene adsorption capacity of *ca.* 608 mg g<sup>-1</sup> at a low  $P/P_0$  of 0.06,<sup>22</sup> the adsorption capacity of A-CNS21 under the same conditions (697 mg g<sup>-1</sup>) is also higher, as well as exhibiting a higher maximum capacity (967 *vs.* 620 mg g<sup>-1</sup>). These remarkable adsorption performance properties of A-CNS21 should result from its valuable textural properties, including its high surface area and the abundance of micropores with matching sizes for the efficient adsorption of both toluene and methanol molecules. These performance properties make A-CNS21 a most suitable adsorbent for the adsorption of toluene and methanol at very low concentrations, thus suggesting its promising use in controlling indoor air contamination of VOCs.

Compared to A-CNS21, AC-PDEB exhibits much lower maximum adsorption capacities towards both toluene and methanol (631 and 572 mg g<sup>-1</sup>, respectively), which should result from its significantly lower total surface area. In the low  $P/P_0$  range ( $P/P_0 < 0.1$ ), AC-PDEB however exhibits a slightly higher methanol adsorption capacity than that of AC-CNS21 while the opposite is found for toluene adsorption. This is reasoned to result from the slightly smaller average micropore size in AC-PDEB, which better matches the adsorption of methanol molecules of a smaller size.

### CO<sub>2</sub> and H<sub>2</sub> adsorption performance

A-CNS21 has also been evaluated for its performance as a sorbent for the adsorption of CO<sub>2</sub> at 0 °C and H<sub>2</sub> at -196 °C.

Fig. 6 shows adsorption isotherms within the pressure range of 0–1 bar at the respective temperatures, along with those of AC-PDEB for comparison. For both CO<sub>2</sub> and H<sub>2</sub>, the desorption isotherms were found to overlap well with the corresponding adsorption isotherms with the absence of hysteresis, thus confirming reversible adsorption and desorption. The adsorption capacity data at 1 bar are summarized in Table 2. At 0 °C and 1 bar, A-CNS21 has a CO<sub>2</sub> adsorption capacity of 26 wt% or 5.8 mmol g<sup>-1</sup> and AC-PDEB has a slightly higher capacity of 28 wt% or 6.4 mmol g<sup>-1</sup>. For CO<sub>2</sub> capture from flue gas, the selectivity of sorbents towards CO<sub>2</sub> relative to other species such as N<sub>2</sub> is also critically important besides the adsorption capacity. The N<sub>2</sub> adsorption isotherm of A-CNS21 is also included in Fig. 6(a), which shows significantly reduced adsorption across the whole relative pressure range. The CO<sub>2</sub>/N<sub>2</sub> Henry selectivity of A-CNS21 is determined to be 10.8, which is high for pure carbon-based sorbents.<sup>13</sup> A similar selectivity value of 11 is found for AC-PDEB.<sup>13</sup>

Among the various available sorbents, porous carbons are the most promising for CO<sub>2</sub> capture due to their easy and low-cost synthesis, resistance to water, and higher adsorption capacities under ambient conditions. At 0 °C and 1 bar, the CO<sub>2</sub> adsorption capacities of porous carbons are generally in the range of 11–39 wt% (see Table S3 in the ESI†), with a predominant dependence on small micropores with sizes of below 0.8 nm.<sup>4d-f</sup> A very high CO<sub>2</sub> adsorption capacity of 38 wt% was reported by Silvestre-Albero *et al.* for a microporous activated carbon obtained from petroleum pitch precursors (BET surface area, 2450 m<sup>2</sup> g<sup>-1</sup>; total pore volume, 1.12 cm<sup>3</sup> g<sup>-1</sup>; micropore volume, 1.03 cm<sup>3</sup> g<sup>-1</sup>).<sup>23</sup> However, it exhibited a very low CO<sub>2</sub>/N<sub>2</sub> selectivity of 2.8. The highest adsorption capacity of 39 wt% for porous carbons was reported by Jaroniec and Wickramaratne for KOH-activated phenolic resin-based carbon spheres,<sup>4f</sup> but with no information given on the selectivity.

The CO<sub>2</sub> adsorption capacities achieved herein for both A-CNS21 and AC-PDEB are high relative to those achieved for many other porous carbons, although they are not the highest. In particular, their overall performances are promising in view of their high CO<sub>2</sub>/N<sub>2</sub> selectivity. Compared to A-CNS21, the slightly higher capacity found for AC-PDEB should result from its slightly higher volume/surface area of micropores with sizes of less than 0.8 nm (0.35 m<sup>3</sup> g<sup>-1</sup> and 903 m<sup>2</sup> g<sup>-1</sup> *vs.* 0.27 cm<sup>3</sup> g<sup>-1</sup> and 741 m<sup>2</sup> g<sup>-1</sup>).

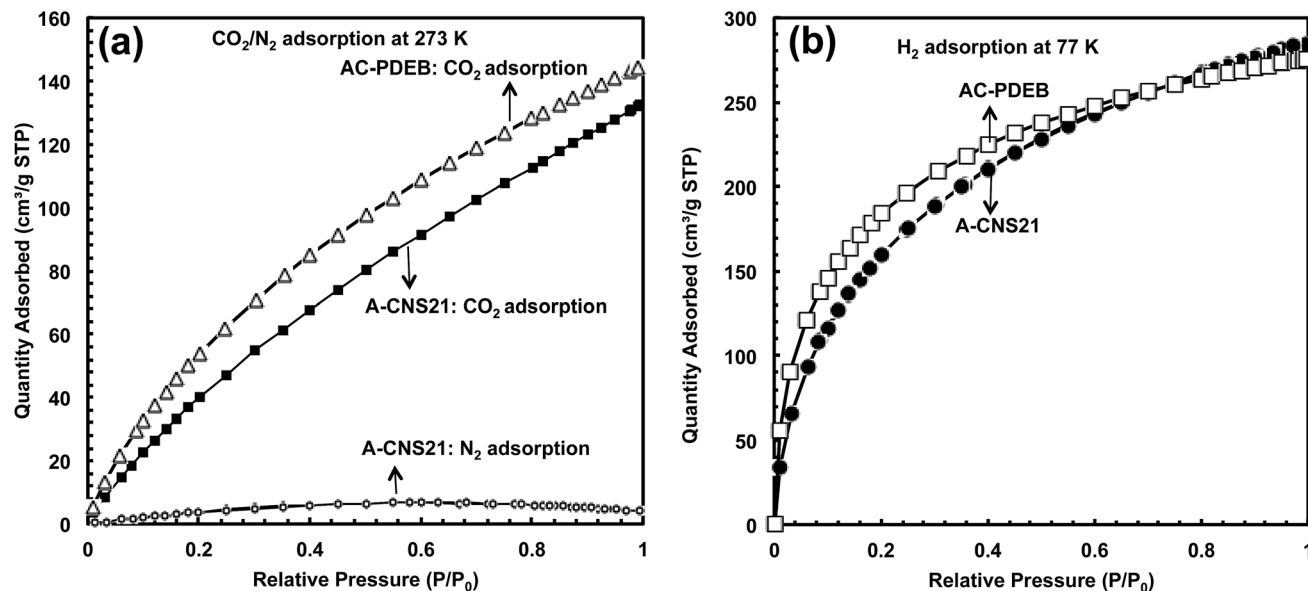


Fig. 6 (a)  $\text{CO}_2/\text{N}_2$  adsorption isotherms at  $0^\circ\text{C}$  for A-CNS21 and AC-PDEB; (b) their  $\text{H}_2$  adsorption isotherms at  $-196^\circ\text{C}$ .

A-CNS21 has a  $\text{H}_2$  adsorption capacity of 2.5 wt% at 1 bar and  $-196^\circ\text{C}$ , with a very similar capacity value of 2.4 wt% found for AC-PDEB. For nanoporous carbons, the  $\text{H}_2$  adsorption capacity shows a predominant dependence on small micropores with sizes of below 1.0 nm.<sup>4a,b</sup> Herein, the two samples have similar volumes and surface areas of micropores with sizes of less than 1.0 nm, with the values of A-CNS21 being slightly higher ( $0.51\text{ cm}^3\text{ g}^{-1}$  and  $1205\text{ m}^2\text{ g}^{-1}$  for A-CNS21;  $0.41\text{ cm}^3\text{ g}^{-1}$  and  $1035\text{ m}^2\text{ g}^{-1}$  for AC-PDEB). Although not the highest, these capacity data are well comparable to those (0.2–3.25 wt%) reported in the literature for various porous carbons (see Table S4 in the ESI†). To the best of our knowledge, the highest  $\text{H}_2$  storage capacity reported for porous carbons at 1 bar and  $-196^\circ\text{C}$  is 3.25 wt% for a MOF-derived, primarily microporous carbon with an exceptionally high surface area ( $3447\text{ m}^2\text{ g}^{-1}$ ) and pore volume ( $1.45\text{ cm}^3\text{ g}^{-1}$ ).<sup>24</sup>

While no dramatic improvements are found herein for A-CNS21 in comparison to AC-PDEB in terms of the  $\text{CO}_2/\text{H}_2$  adsorption capacities due to their primary dependences on small micropores, we reason that the adsorption kinetics can be improved for A-CNS21 under circumstances where the diffusion of the adsorbate molecules in the micropores is an issue, such as in viscous systems. The hierarchical pore structures with abundant large meso-/macropores in A-CNS21 may offer faster diffusion of adsorbate molecules into micropores and thus offer the advantages of improved adsorption kinetics in those cases. This is to be further investigated in our subsequent studies.

## Conclusions

A new catalytic emulsion polymerization strategy employing DEB as the monomer precursor has been successfully demonstrated for the efficient synthesis of ultra-small carbon nanospheres with uniform tunable sizes (11–38 nm) in a gram scale.

By simply changing the DEB feed concentration in the emulsion polymerization process, polymer nanospheres (PNS11, PNS21 and PNS38) with uniform tunable sizes have been conveniently obtained with a high monomer conversion. Carbonization of the PNSs after hydrothermal treatment without activation gives rise to the corresponding carbon nanospheres (CNS11, CNS21 and CNS38) with well-retained nanosphere morphologies and sizes. Carbonization of PNS21 in the presence of KOH renders effectively A-CNS21 with a very high surface area ( $2360\text{ m}^2\text{ g}^{-1}$ ) and pore volume ( $1.98\text{ cm}^3\text{ g}^{-1}$ ), as well as hierarchical micro-/meso-/macropore structures which result from nanosphere packing/aggregation. A-CNS21 demonstrates outstanding high-rate supercapacitive performance, and sorption performance towards the storage of  $\text{CO}_2/\text{H}_2$  and the capture of VOCs. It exhibits a very high specific capacitance ( $305\text{ F g}^{-1}$  at  $0.1\text{ A g}^{-1}$ ) and a remarkably high capacitance retention (72% retention at  $10\text{ A g}^{-1}$ ), which compare well with the best results achieved in the literature and are much superior in comparison with the results of AC-PDEB, the activated carbon control sample. A-CNS21 also exhibits superior maximum adsorption capacities towards toluene and methanol vapors ( $967$  and  $937\text{ mg g}^{-1}$ , respectively, at a  $P/P_0$  of 0.99). Among the various high-performance adsorbents reported to date, it exhibits the highest adsorption capacities towards the two VOCs at low concentrations ( $866$  and  $366\text{ mg g}^{-1}$ , respectively, at a  $P/P_0$  of 0.1). In addition, A-CNS21 also exhibits high  $\text{CO}_2$  (1 bar and  $0^\circ\text{C}$ ) and  $\text{H}_2$  (1 bar and  $-196^\circ\text{C}$ ) adsorption capacities (26 and 2.5 wt%, respectively). Given the high efficiency and easy scalability of the emulsion polymerization technique with the use of all commercially available precursors, as well as the outstanding performances of the resulting carbon nanospheres, we expect potential applications of this novel technique for the large-scale tailored synthesis of well-defined ultra-small carbon nanospheres.

## Acknowledgements

This work was financially supported by grants from the Canada Research Chair (Grant # 220084 and 230723) and the Natural Science and Engineering Research Council of Canada (Grant # RGPIN-2015-03815 and 477901-2015).

## Notes and references

- (a) J. Liu, N. P. Wickramaratne, S. Z. Qiao and M. Jaroniec, *Nat. Mater.*, 2015, **14**, 763–774; (b) P. Zhang, Z.-A. Qiao and S. Dai, *Chem. Commun.*, 2015, **51**, 9246–9256; (c) A. D. Roberts, X. Li and H. Zhang, *Chem. Soc. Rev.*, 2014, **43**, 4341–4356; (d) A. Nieto-Márquez, R. Romero, A. Romero and J. L. Valverde, *J. Mater. Chem.*, 2011, **21**, 1664–1672.
- (a) J. Lee, J. Kim and T. Hyeon, *Adv. Mater.*, 2006, **18**, 2073–2094; (b) H. Nishihara and T. Kyotani, *Adv. Mater.*, 2012, **24**, 4473–4498; (c) Y. Xia, Z. Yang and R. Mokaya, *Nanoscale*, 2010, **2**, 639–659; (d) B. Fang, J. H. Kim, M.-S. Kim and J.-S. Yu, *Acc. Chem. Res.*, 2013, **46**, 1397–1406; (e) M. Antonietti, N. Fechler and T.-P. Fellingner, *Chem. Mater.*, 2014, **26**, 196–210; (f) Y. Zhai, Y. Dou, D. Zhao, P. F. Fulvio, R. T. Mayes and S. Dai, *Adv. Mater.*, 2011, **23**, 4828–4850.
- Representative papers on effects of micropores on electrocapacitive energy storage: (a) J. Chmiola, G. Yushin, Y. Gogotsi, C. Portet, P. Simon and P. L. Taberna, *Science*, 2006, **313**, 1760–1763; (b) C. Largeot, C. Portet, J. Chmiola, P.-L. Taberna, Y. Gogotsi and P. Simon, *J. Am. Chem. Soc.*, 2008, **130**, 2730–2731; (c) J. Chmiola, C. Largeot, P.-L. Taberna, P. Simon and Y. Gogotsi, *Angew. Chem., Int. Ed.*, 2008, **47**, 3392–3395.
- Representative papers on effects of micropores on H<sub>2</sub>/CO<sub>2</sub> storage: (a) Y. Gogotsi, R. K. Dash, G. Yushin, T. Yildirim, G. Laudisio and J. E. Fischer, *J. Am. Chem. Soc.*, 2005, **127**, 16006–16007; (b) G. Yushin, R. Dash, J. Jagiello, J. E. Fischer and Y. Gogotsi, *Adv. Funct. Mater.*, 2006, **16**, 2288–2293; (c) N. Texier-Mandoki, J. Dentzer, T. Piquero, S. Saadallah, P. David and C. Vix-Guterl, *Carbon*, 2004, **42**, 2735–2777; (d) V. Presser, J. McDonough, S.-H. Yeon and Y. Gogotsi, *Energy Environ. Sci.*, 2011, **4**, 3059–3066; (e) J. Silvestre-Alberto, A. Wahby, A. Sepúlveda-Escribano, M. Martínez-Escandell, K. Kaneko and F. Rodríguez-Reinoso, *Chem. Commun.*, 2011, **47**, 6840–6842; (f) N. P. Wickramaratne and M. Jaroniec, *J. Mater. Chem. A*, 2013, **1**, 112–116.
- Representative examples on hard-templating strategy: (a) A. B. Fuertes, *J. Mater. Chem.*, 2003, **13**, 3085–3088; (b) T.-W. Kim, P.-W. Chung, I. I. Slowing, M. Tsunoda, E. S. Yeung and V. S.-Y. Lin, *Nano Lett.*, 2008, **8**, 3724–3727; (c) Z. Lei, N. Christov, L. L. Zhang and X. S. Zhao, *J. Mater. Chem.*, 2011, **21**, 2274–2281; (d) J. Schuster, G. He, B. Mandlmeier, T. Yim, K. T. Lee, T. Bein and L. F. Nazar, *Angew. Chem., Int. Ed.*, 2012, **51**, 3591–3595; (e) Z. Sun, Y. Liu, B. Li, J. Wei, M. Wang, Q. Yue, Y. Deng, S. Kaliaguine and D. Zhao, *ACS Nano*, 2013, **7**, 8706–8714; (f) Z.-A. Qiao, B. Guo, A. J. Binder, J. Chen, G. M. Veith and S. Dai, *Nano Lett.*, 2013, **13**, 207–212.
- Representative examples on self-assembly strategy: (a) Y. Fang, D. Gu, Y. Zou, Z. Wu, F. Li, R. Che, Y. Deng, B. Tu and D. Zhao, *Angew. Chem., Int. Ed.*, 2010, **49**, 7987–7991; (b) J. Liu, T. Yang, D.-W. Wang, G. Q. Lu, D. Zhao and S. Z. Qiao, *Nat. Commun.*, 2013, **4**, 2798; (c) T. Yang, J. Liu, R. Zhou, Z. Chen, H. Xu, S. Z. Qiao and M. J. Monteiro, *J. Mater. Chem. A*, 2014, **2**, 18139–18146; (d) J. Wang, H. Liu, J. Diao, X. Gu, H. Wang, J. Rong, B. Zong and D. S. Su, *J. Mater. Chem. A*, 2015, **3**, 2305–2313; (e) J. Tang, J. Liu, C. Li, Y. Li, M. O. Tade, S. Dai and Y. Yamauchi, *Angew. Chem., Int. Ed.*, 2015, **54**, 588–593; (f) A.-H. Lu, W.-C. Li, G.-P. Hao, B. Spliethoff, H.-J. Bongard, B. B. Schaack and F. Schüth, *Angew. Chem., Int. Ed.*, 2010, **49**, 1615–1618; (g) S. Wang, W.-C. Li, G.-P. Hao, Y. Hao, Q. Sun, X.-Q. Zhang and A.-H. Lu, *J. Am. Chem. Soc.*, 2011, **133**, 15304–15307; (h) S. Wang, W.-C. Li, L. Zhang, Z.-Y. Jin and A.-H. Lu, *J. Mater. Chem. A*, 2014, **2**, 4406–4412; (i) F. Xu, Z. Tang, S. Huang, L. Chen, Y. Liang, W. Mai, H. Zhong, R. Fu and D. Wu, *Nat. Commun.*, 2015, **6**, 7221.
- Representative examples on extended Stober strategy: (a) J. Liu, S. Z. Qiao, H. Liu, J. Chen, A. Orpe, D. Zhao and G. Q. Lu, *Angew. Chem., Int. Ed.*, 2011, **50**, 5947–5951; (b) J. Choma, D. Jamiola, K. Augustynek, M. Marszewski, M. Gao and M. Jaroniec, *J. Mater. Chem.*, 2012, **22**, 12636–12642; (c) J. Ludwinowicz and M. Jaroniec, *Carbon*, 2015, **82**, 297–303; (d) N. P. Wickramaratne and M. Jaroniec, *ACS Appl. Mater. Interfaces*, 2013, **5**, 1849–1855; (e) N. P. Wickramaratne, V. S. Perera, J. M. Ralph, S. D. Huang and M. Jaroniec, *Langmuir*, 2013, **29**, 4032–4038; (f) J. Choma, W. Fahrenholz, D. Jamiola, J. Ludwinowicz and M. Jaroniec, *Microporous Mesoporous Mater.*, 2014, **185**, 197–203; (g) J. Qian, M. Liu, L. Gan, P. K. Tripathi, D. Zhu, Z. Xu, Z. Hao, L. Chen and D. S. Wright, *Chem. Commun.*, 2013, **49**, 3043–3045; (h) X. Ma, L. Gan, M. Liu, P. K. Tripathi, Y. Zhao, Z. Xu, D. Zhu and L. Chen, *J. Mater. Chem. A*, 2014, **2**, 8407–8415; (i) J. Zhao, W. Niu, L. Zhang, H. Cai, M. Han, Y. Yuan, S. Majeed, S. Anjum and G. Xu, *Macromolecules*, 2013, **46**, 140–145; (j) Z. Xu and Q. Guo, *Carbon*, 2013, **52**, 464–467; (k) V. G. Pol, L. K. Shrestha and K. Ariga, *ACS Appl. Mater. Interfaces*, 2014, **6**, 10649–10655; (l) J. Wang, L. Yao, C. Ma, X. Guo, W. Qiao, L. Ling and D. Long, *ACS Appl. Mater. Interfaces*, 2016, **8**, 4851–4861; (m) K. Ai, Y. Liu, C. Ruan, L. Lu and G. Lu, *Adv. Mater.*, 2013, **25**, 998–1003.
- Representative examples on hydrothermal carbonization strategy: (a) B. Hu, K. Wang, L. Wu, S.-H. Yu, M. Antonietti and M.-M. Titirici, *Adv. Mater.*, 2010, **22**, 813–828; (b) X. Sun and Y. Li, *Angew. Chem., Int. Ed.*, 2004, **43**, 597–601; (c) Y. Shin, L.-Q. Wang, I.-T. Bae, B. W. Arey and G. J. Exarhos, *J. Phys. Chem. C*, 2008, **112**, 14236–14240; (d) N. Baccile, M. Antonietti and M.-M. Titirici, *ChemSusChem*, 2010, **3**, 246–253; (e) T.-P. Fellingner, R. J. White, M.-M. Titirici and M. Antonietti, *Adv. Funct. Mater.*, 2012, **22**, 3254–3260; (f) P. Zhang, J. Yuan, T.-P. Fellingner, M. Antonietti, H. Li and Y. Wang, *Angew. Chem., Int. Ed.*,

- 2013, **52**, 6028–6032; (g) Y. Gong, Z. Wei, J. Wang, P. Zhang, H. Li and Y. Wang, *Sci. Rep.*, 2014, **4**, 6349.
- 9 Representative examples on emulsion polymerization strategy: (a) J. Jang and H. Yoon, *Small*, 2005, **1**, 1195–1199; (b) W.-K. Oh, H. Yoon and J. Jang, *Biomaterials*, 2010, **31**, 1342–1348; (c) S. Lee, K.-Y. Shin and J. Jang, *Nanoscale*, 2015, **7**, 9646–9654; (d) Y. Ouyang, H. Shi, R. Fu and D. Wu, *Sci. Rep.*, 2013, **3**, 1430; (e) F. Xu, R. Cai, Q. Zeng, C. Zou, D. Wu, F. Li, X. Lu, Y. Liang and R. Fu, *J. Mater. Chem.*, 2011, **21**, 1970–1976.
- 10 (a) S. Tanaka, H. Nakao, T. Mukai, Y. Katayama and Y. Miyake, *J. Phys. Chem. C*, 2012, **116**, 26791–26799; (b) X. Huang, S. Kim, M. S. Heo, J. E. Kim, H. Suh and I. Kim, *Langmuir*, 2013, **29**, 12266–12274; (c) B. Chang, Y. Guo, Y. Li, H. Yin, S. Zhang, B. Yang and X. Dong, *J. Mater. Chem. A*, 2015, **3**, 9565–9577.
- 11 (a) C. Portet, G. Yushin and Y. Gogotsi, *J. Electrochem. Soc.*, 2008, **155**, A531–A536; (b) C. R. Pérez, S.-H. Yeon, J. Ségalini, V. Presser, P.-L. Taberna, P. Simon and Y. Gogotsi, *Adv. Funct. Mater.*, 2013, **23**, 1081–1089.
- 12 S. Y. Lim, W. Shen and Z. Gao, *Chem. Soc. Rev.*, 2015, **44**, 362–381.
- 13 M. Grundy and Z. Ye, *J. Mater. Chem. A*, 2014, **2**, 20316–20330.
- 14 (a) Z. Dong and Z. Ye, *Macromolecules*, 2012, **45**, 5020–5031; (b) Z. Dong and Z. Ye, *Adv. Synth. Catal.*, 2014, **356**, 3401–3414; (c) Z. Dong and Z. Ye, *Appl. Catal., A*, 2015, **489**, 61–71.
- 15 J. Huber and S. Mecking, *Macromolecules*, 2010, **43**, 8718–8723.
- 16 S. S. Sakhawat, Ejaz-ur-Rehman, Effect of temperature and aprotic solvents on the CMC of sodium dodecyl sulphate, in *Interactions of Water in Ionic and Nonionic Hydrates*, ed. H. Kleeberg, Springer-Verlag, Berlin, Heidelberg, 1987, pp. 251–255.
- 17 K. S. W. Sing, D. H. Everett, R. A. W. Haul, L. Moscou, R. A. Pierotti, J. Rouquérol and T. Siemieniewska, *Pure Appl. Chem.*, 1985, **57**, 603–619.
- 18 L. Xu, J.-W. McGraw, F. Gao, M. Grundy, Z. Ye, Z. Gu and J. L. Shepherd, *J. Phys. Chem. C*, 2013, **117**, 10730–10742.
- 19 (a) Q. Zhao, T.-P. Fellingner, M. Antonietti and J. Yuan, *J. Mater. Chem. A*, 2013, **1**, 5113–5120; (b) D. Puthusseri, V. Aravindan, S. Madhavi and S. Ogale, *Energy Environ. Sci.*, 2004, **7**, 728–735.
- 20 L. Xu, L. Huang, Z. Ye, N. Meng, Y. Shu and Z. Gu, *Macromol. Rapid Commun.*, 2017, **3**, 1600608.
- 21 T. Ben, H. Ren, S. Ma, D. Cao, J. Lan, X. Jing, W. Wang, J. Xu, F. Deng, J. M. Simmons, S. Qiu and G. Zhu, *Angew. Chem., Int. Ed.*, 2009, **48**, 9457–9460.
- 22 F. Xu, S. Xian, Q. Xia, Y. Li and Z. Li, *Adsorpt. Sci. Technol.*, 2013, **31**, 325–339.
- 23 A. Wahby, J. M. Ramos-Fernández, M. Martínez-Escandell, A. Sepúlveda-Escribano, J. Silvestre-Albero and F. Rodríguez-Reinoso, *ChemSusChem*, 2010, **3**, 974–981.
- 24 S. J. Yang, T. Kim, J. H. Im, Y. S. Kim, K. Lee, H. Jung and C. R. Park, *Chem. Mater.*, 2012, **24**, 464–470.